Nanoscale

PAPER

View Article Online
View Journal | View Issue

Check for updates

Cite this: *Nanoscale*, 2020, **12**, 10647

Wafer-scale 2D $PtTe_2$ layers for high-efficiency mechanically flexible electro-thermal smart window applications†

Emmanuel Okogbue,[a,b] Tae-Jun Ko,[a] Sang Sub Han,[a,c] Mashiyat Sumaiya Shawkat,[a,b] Mengjing Wang,[a] Hee-Suk Chung,[d] Kyu Hwan Oh[c] and Yeonwoong Jung *[a,b,e]

Two-dimensional (2D) transition metal dichalcogenide (TMD) layers have gained increasing attention for a variety of emerging electrical, thermal, and optical applications. Recently developed metallic 2D TMD layers have been projected to exhibit unique attributes unattainable in their semiconducting counterparts; *e.g.*, much higher electrical and thermal conductivities coupled with mechanical flexibility. In this work, we explored 2D platinum ditelluride (2D $PtTe_2$) layers – a relatively new class of metallic 2D TMDs – by studying their previously unexplored electro-thermal properties for unconventional window applications. We prepared wafer-scale 2D $PtTe_2$ layer-coated optically transparent and mechanically flexible willow glasses *via* a thermally-assisted tellurization of Pt films at a low temperature of 400 °C. The 2D $PtTe_2$ layer-coated windows exhibited a thickness-dependent optical transparency and electrical conductivity of $>10^6$ S m^{-1} – higher than most of the previously explored 2D TMDs. Upon the application of electrical bias, these windows displayed a significant increase in temperature driven by Joule heating as confirmed by the infrared (IR) imaging characterization. Such superior electro-thermal conversion efficiencies inherent to 2D $PtTe_2$ layers were utilized to demonstrate various applications, including thermochromic displays and electrically-driven defogging windows accompanying mechanical flexibility. Comparisons of these performances confirm the superiority of the wafer-scale 2D $PtTe_2$ layers over other nanomaterials explored for such applications.

Received 4th March 2020,
Accepted 14th April 2020

DOI: 10.1039/d0nr01845g

rsc.li/nanoscale

Introduction

Electro-thermal materials that can convert electric inputs into thermal energy have been explored for a wide range of applications such as smart textiles and wearable/portable heaters. Particularly, such materials in thin-film forms which retain good optical transparency and mechanical flexibility upon Joule heating are attractive for "smart windows" with electrically-driven defogging and heat-retention ability.[1,2] To date, indium tin oxide (ITO) has been extensively employed for such applications benefiting from its high optical transparency in the visible light regime due to its large bandgap energy.[3,4] Despite the combined advantage of high electrical conductivity and optical transparency, ITO is intrinsically brittle and fragile with very limited flexibility, stretchability, and bendability.[2,4,5] Alternatively, substantial efforts have been made to explore nanostructured electro-thermal materials with superior mechanical deformability and adaptability, such as one-dimensional (1D) metallic materials such as silver (Ag) nanowires and multi-walled carbon nanotubes (MWCNTs)[6,7] or 2D materials such as graphene or graphene oxide.[2,8,9] These materials in liquid dispersion forms are directly "drop-cast" onto flexible windows, which results in randomly-networked structures where electron transports occur in a percolation manner.[10] Accordingly, they often suffer from loose interfacial contacts with the underlying windows, which leads to the degradation of electro-thermal efficiency upon repeated electrical biasing as previously verified.[11–14] Recently, 2D transition metal dichalcogenide (TMD) layers are gaining increasing attention for a variety of emerging applications which require combined attributes of high mechanical flexibility and electrical/thermal transports.[15–19] Compared to their semiconductor

[a]*NanoScience Technology Center, University of Central Florida, Orlando, Florida 32826, USA. E-mail: yeonwoong.jung@ucf.edu*
[b]*Department of Electrical and Computer Engineering, University of Central Florida, Orlando, Florida 32816, USA*
[c]*Department of Materials Science and Engineering, Seoul National University, Seoul, 08826, South Korea*
[d]*Analytical Research Division, Korea Basic Science Institute, Jeonju 54907, South Korea*
[e]*Department of Materials Science and Engineering, University of Central Florida, Orlando, Florida 32826, USA*

†Electronic supplementary information (ESI) available. See DOI: 10.1039/d0nr01845g

counterparts, which have been mainly developed for digital electronics,[20,21] metallic 2D TMD layers are particularly suitable for electro-thermal applications owing to their intrinsically higher electrical conductivity.[17,21–23] The direct chemical growth of highly metallic 2D TMD layers on flexible and transparent windows avoiding conventional drop-casting approaches should offer distinct advantages in achieving structurally/chemically robust interfaces, and thereby the desired electro-thermal properties. While chemical vapor deposition (CVD) has extensively been employed for the scalable growth of 2D TMD layers,[24,25] electro-thermal applications in mechanically flexible forms have been limited with most 2D TMDs due to their high CVD growth temperature.[20,25–27]

In this work, we investigated the electro-thermal properties of 2D platinum ditelluride (2D $PtTe_2$) layers – a relatively unexplored class of metallic 2D TMDs with tunable electronic properties.[21,28] We directly grew wafer-scale 2D $PtTe_2$ layers on mechanically flexible and optically transparent window materials *via* a thermally-assisted conversion (TAC) of Pt thin films at 400 °C. We experimentally confirmed that they exhibit extremely high electrical conductivity superior to nearly all previously reported 2D TMD layers accompanying thickness-dependent optical transparency. Furthermore, we identified their electrical bias-dependent temperature increase through infrared (IR) characterization and verified excellent electro-thermal properties. By taking advantage of these superior properties, we explored their applications in electro-thermal smart windows of unconventional forms. Particularly, we achieved proof-of-concept demonstrations of thermochromic displays with electrically-tunable color and mechanically-flexible defogging windows.

Experimental

Synthesis of 2D $PtTe_2$ layers

2D $PtTe_2$ layers were grown on various substrates by a two-step TAC process. Pt films of controlled thickness were deposited on the substrates using an electron beam evaporator (Temescal) at a deposition rate of 0.10 Å s^{-1}. The Pt-deposited substrate is placed in the middle zone in a horizontal quartz tube furnace (Lindberg/Blue M Mini-Mite) with an alumina boat containing tellurium (Te) powder loaded in the upstream side. The quartz tube is pumped down to a pressure of 25 mTorr and purged with argon (Ar) to remove residual gases and moisture. The furnace is heated to 400 °C in 50 minutes and held there for 50 minutes under a continuous flow of Ar, followed by a natural cool-down to room temperature.

Electrical and electro-thermal characterization

For electrical characterization, Au top electrodes were deposited on 2D $PtTe_2$ layers/WG samples yielding two-terminal configurations. Sheet resistance measurements were carried out using a four-point probe station (Signatone). For electro-thermal characterization, fabricated devices were connected to a power supply (Tek Power TP3005T) and their bias-dependent IR images were obtained using an IR camera (FLIR C2) at room temperature.

Optical transmittance and water contact angle characterization

Optical transmittances of 2D $PtTe_2$ layer-based window samples were characterized using ultraviolet-vis (UV-Vis) spectroscopy (Cary WinUV spectrometer) in the wavelength range of 200–800 nm. Water contact angle measurements were performed using a goniometer (Rame Hart 90-U3-PRO) where water droplets of the same volume were used to ensure measurement uniformity.

TEM, STEM and XPS characterization

X-ray photoelectron spectroscopy (XPS) characterization was carried out using Thermo VG Scientific K-α system with an Al Kα ray source under ultrahigh vacuum conditions. The binding energy of C 1s, 284.5 eV, and a Shirley-type background were used to calibrate all the XPS peaks, and the peak fittings were completed using a Voigt function. Transmission electron microscopy (TEM) and scanning transmission electron microscopy (STEM) characterization were performed using JEOL ARM200F FED-TEM/STEM with a Cs (spherical aberration) corrector. Focused ion beam (FIB) milling and lift-out techniques were used to prepare cross-sectional TEM samples using a Quanta 2D FEG, FEI. All TEM/STEM operations were performed at an accelerating voltage of 200 kV.

Defogging measurements

For high humidity defogging measurements, a commercial vaporizer was used to supply water vapor onto the surface of samples. For low humidity defogging measurements, the samples were placed above a water-containing beaker, which was heated to about 80 °C. The temperature of the lab where these measurements were performed was 23 °C.

Results

Fig. 1a presents a schematic illustration of the growth of wafer-scale 2D $PtTe_2$ layers on various substrates, which is carried out in two-step procedures; Pt films of controlled thickness are deposited on growth substrates (*e.g.*, silicon dioxide/silicon (SiO_2/Si), willow glass (WG), and mica) followed by thermal tellurization at 400 °C, similar to our previous studies.[29–32] The Pt-deposited growth substrate and tellurium powder are placed in the mid- and up-stream side of a CVD tube furnace, respectively. The tube is pumped down to a base pressure of 25 mTorr followed by Ar gas purging and is subsequently filled with Ar gas of 100 sccm (standard cubic centimeter per minute). The temperature of the furnace center zone is maintained at 400 °C for 50 min according to the temperature profile shown in Fig. S1 (ESI†) yielding the conversion of Pt to 2D $PtTe_2$ layers. Fig. 1b shows a representative image of wafer-scale 2D $PtTe_2$ layers as-grown on a SiO_2/Si substrate. Prior to investigating the electro-thermal properties, we first characterized their structural and chemical integrity *via* TEM/STEM,

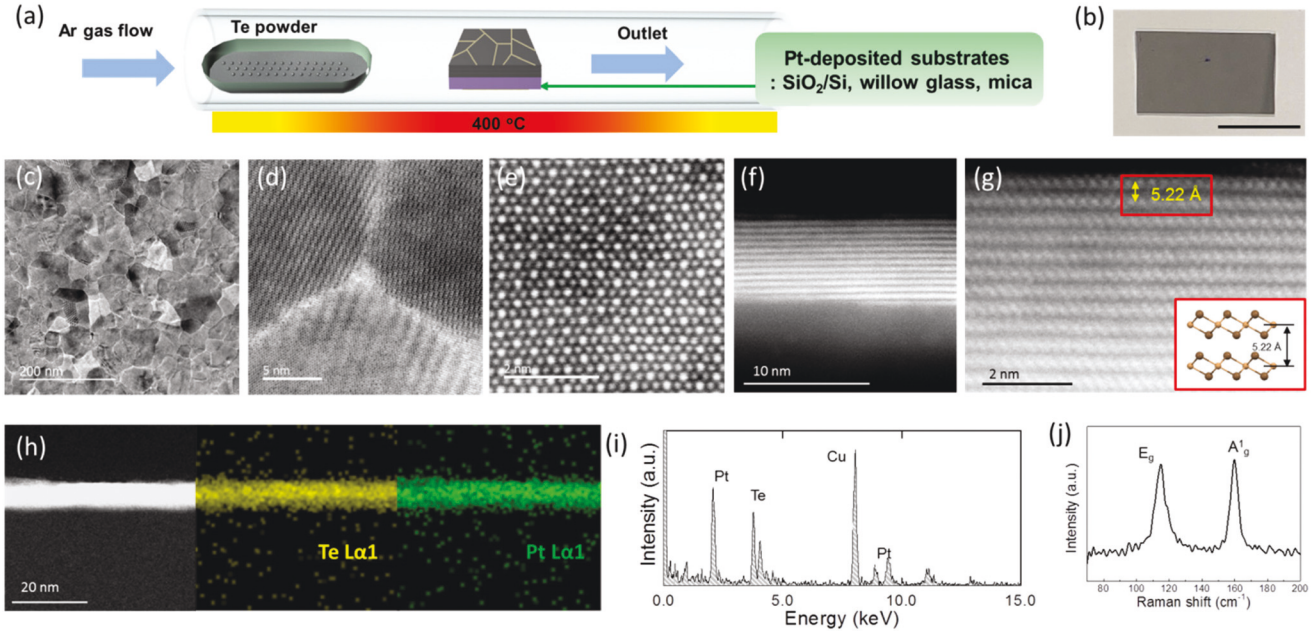

Fig. 1 (a) Schematic illustration of the low-temperature growth of wafer-scale 2D $PtTe_2$ layers on various substrates. (b) Optical image of wafer-scale 2D $PtTe_2$ layers on a SiO_2/Si substrate. The scale bar is 2 cm. (c) Low magnification TEM image showing the well-defined grains. (d, e) High resolution TEM images showing; (d) well-defined grain boundaries, and (e) atomic arrangement showing 1T stacking. (f, g) High-resolution cross-sectional TEM image showing; (f) horizontal $PtTe_2$ layers, and (g) well-resolved 2D layers with an interlayer spacing of 5.22 Å. (h) Cross-section EDS mapping images showing the spatial distribution of Pt and Te. (i) EDS spectrum. (j) Raman profile.

Raman spectroscopy, and energy-dispersive X-ray spectroscopy (EDS). Fig. 1c shows a representative low-magnification TEM image of 2D $PtTe_2$ layers grown on a SiO_2/Si substrate, revealing their continuous film morphology composed of a large number of crystalline grains. Fig. 1d presents a high-resolution TEM (HRTEM) image focused on one of the multi-grained regions, revealing well-resolved grain boundaries across the grains. Fig. 1e is the atomic resolution HRTEM image of a selected grain where the bright/dark atomic arrangement confirms the highly-crystalline structure of the 2D $PtTe_2$ grain in the 1T phase.[21,33] Cross-sectional HRTEM characterization was further employed to identify the crystallographic structure and layer orientation of the as-grown 2D $PtTe_2$ layers. Fig. 1f shows a representative HRTEM image of 2D $PtTe_2$ multilayers in a cross-sectional view, exhibiting that individual 2D layers are vertically-stacked on top of each other, retaining horizontal alignment without discontinuity. Fig. 1g further visualizes the interlayer structure of the corresponding sample, from which the well-resolved van der Waals spacing of ~5.22 Å was determined. The inset image illustrates the atomic structure model corresponding to the red boxed region, confirming the 1T-phased hexagonal configuration of 2D $PtTe_2$ layers consistent with previous studies.[21,28] Fig. 1h shows the EDS elemental mapping image of the same sample, visualizing the highly uniform spatial distribution of constituting Pt and Te elements. Fig. 1i presents the EDS spectrum corresponding to Fig. 1h, which indicates the atomic ratio of Pt : Te $\simeq$ 1 : 2 validating the growth of stoichiometric 2D $PtTe_2$ layers.[21,27] Lastly, Fig. 1j exhibits the Raman profile obtained from a sample of as-grown 2D $PtTe_2$ layers on a SiO_2/Si substrate. Two characteristic peaks are observed at t $\simeq$115 cm^{-1} and $\simeq$159 cm^{-1}, which correspond to the in-plane (E_g) and out-of-plane (A_{1g}) vibration modes of 1T-phased $PtTe_2$, respectively.[28,34] Note that the growth temperature for these 2D $PtTe_2$ layers is 400 °C, much lower than those of other 2D TMDs, thus offering great compatibility for their direct growth on various glass substrates.

Projecting their applications for smart windows, we also grew wafer-scale 2D $PtTe_2$ layers on transparent substrates by employing the same growth procedure and investigated their optical transparency and electro-thermal properties. We first adopted WG substrates which are optically transparent, electrically insulating, and mechanically flexible. Fig. 2a shows the optical images of 2D $PtTe_2$ layers prepared with varying Pt thicknesses, revealing UCF logos on the background. The images show decreasing optical transparency with increasing Pt thickness, *i.e.*, 0 nm, 0.75 nm, 1.5 nm, and 3 nm from top-to-bottom. We verified that the tellurization of Pt films increased their initial thickness by ~5 times through conversion to 2D $PtTe_2$ layers, as presented in Fig. S2 (ESI†). Prior to further optical or electrical characterization, we first confirmed the successful growth of 2D $PtTe_2$ layers on WG substrates by employing XPS characterization. Fig. 2b and c show the XPS profile specific to the core energy levels of Pt and Te elements from a sample of the as-grown 2D $PtTe_2$ layers/WG, respectively. The XPS profile in Fig. 2b exhibits the Pt-4f core level peaks at 72.2 eV and 75.5 eV corresponding to 4f 7/2 and 4f 5/2, respectively, which well agrees with previous studies on the XPS characterization of 2D $PtTe_2$ layers.[21,35–37] The XPS profile

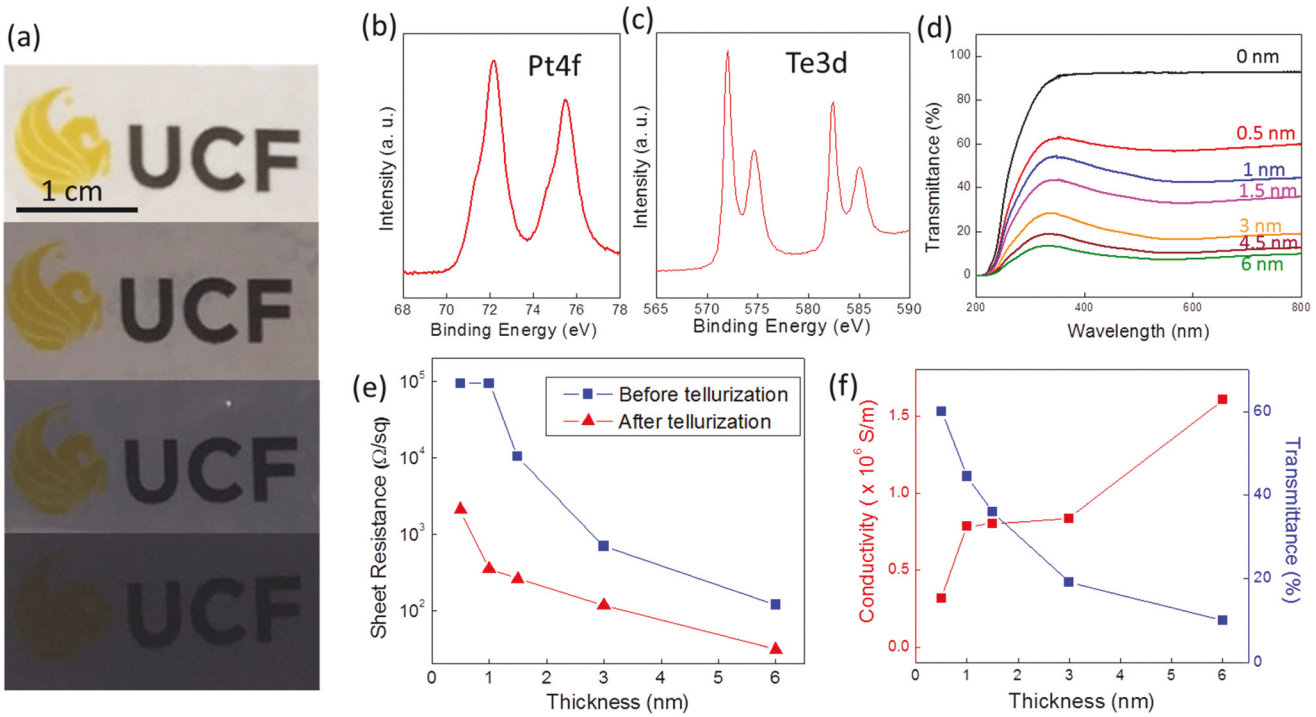

Fig. 2 (a) Digital images of 2D $PtTe_2$ layers/WG samples prepared by the tellurization of 0 nm, 0.75 nm, 1.5 nm, and 3 nm thick Pt films (top to bottom). (b, c) XPS characterization of (b) Pt 4f and (c) Se 3d core levels obtained from 2D $PtTe_2$ layers/WG. (d) Optical transmittance of 2D $PtTe_2$ layers/WG in the ultraviolet–visible wavelength region. (e) Sheet resistance of Pt films before and after tellurization as a function of their thickness. (f) Sheet resistance and optical transmittance of 2D $PtTe_2$ layers prepared with Pt films of various thicknesses.

in Fig. 2c exhibits Te-3d core-level peaks at 576 eV and 586.3 eV corresponding to Te(IV) species as well as additional peaks at 573 eV and 583.4 eV corresponding to Te(0), which is also consistent with previous studies.[35,38] We also conducted the XPS characterization of 2D $PtTe_2$ layers grown on SiO_2/Si substrates and verified nearly identical peak characteristics, which further confirms that our growth process is insensitive to growth substrates (Fig. S3, ESI†). The optical properties of 2D $PtTe_2$ layers/WG substrates were investigated by UV-Vis spectroscopy characterization. Fig. 2d shows the optical transmittance of 2D $PtTe_2$ layers directly grown on WG substrates prepared with varying Pt thicknesses. 2D $PtTe_2$ layers grown with Pt of 1.5 nm and below present $\gtrsim$40% optical transmittance in the regime of visible light wavelength (380 nm–740 nm) while the transmittance decreases with increasing thickness, similar to observations with other 2D TMDs.[39,40] The corresponding optical absorbance spectra showing thickness-dependent increasing absorbance are presented in Fig. S4, ESI.† The electrical properties of these samples were also characterized by a four-point probing technique which deduces their sheet resistance. Fig. 2e presents sheet resistance values of the as-deposited Pt thin films before and after tellurization as a function of Pt thickness. It is noted that the grown 2D $PtTe_2$ layers (*i.e.*, after tellurization) exhibit orders of magnitude lower sheet resistances compared to those of Pt-only states (*i.e.*, before tellurization). Such low sheet resistance values are essential for an efficient electro-thermal energy conversion as the Joule-heating efficiency is expressed by $P = V^2/R_s$ where P is the power, V is the voltage, and R_s is the sheet resistance. Fig. 2f summarizes the optical transmittance and electrical conductivity of 2D $PtTe_2$ layers grown on WG substrates as a function of Pt thickness. The plots evidence that fairly high electrical conductivity (*i.e.*, $\gtrsim 5 \times 10^5$ S m^{-1}) is achieved accompanying good optical transmittance ($\gtrsim$40%) for the samples prepared with Pt of ~1 nm.

Electro-thermal performances of 2D $PtTe_2$ layers grown on WG substrates were identified by measuring their temperature change upon electrical biasing. Two-terminal gold (Au) top electrodes (100 nm thickness) were deposited on 2D $PtTe_2$ layers/WG samples which were electrically-biased through a DC regulated power supply. The temperature rise of the samples introduced by various voltages was confirmed by monitoring their IR images using an IR camera (FLIR). Fig. 3a and b show bias-dependent IR images of 2D $PtTe_2$ layers prepared with two different Pt thicknesses of 0.5 nm and 1 nm, respectively. It is noted that their temperature steadily increases with increasing sample thickness and voltage amplitude while the maximum applied voltage was kept below 30 V to ensure safety and real-life applicability; *i.e.*, for the 2D $PtTe_2$ layers prepared with 0.5 nm Pt thickness (Fig. 3a), the temperature increased from 28.5 °C at 0 V to a maximum temperature (T_{max}) of 49.1 °C at 30 V while the sample prepared with 1 nm Pt exhibited a T_{max} of 160.2 °C at 15 V (Fig. 3b). Fig. 3c presents voltage-dependent temperature variation for 2D $PtTe_2$ layers/WG samples prepared with varying Pt thicknesses. We note that even the samples with sufficiently large optical trans-

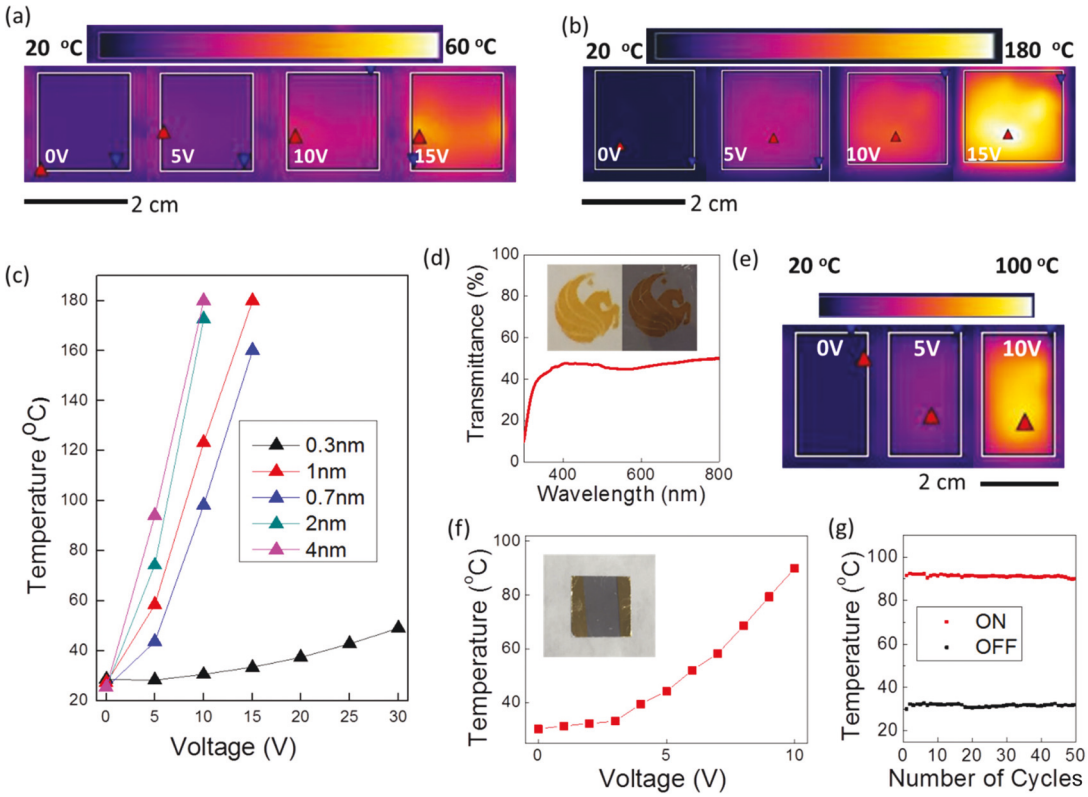

Fig. 3 (a, b) IR images of 2D $PtTe_2$ layers/WG samples prepared with Pt films of (a) 0.5 nm and (b) 1 nm thickness. (c) Voltage-dependent temperature profiles of 2D $PtTe_2$ layers/WG samples prepared with Pt films of various thicknesses. (d) Optical transmittance of 2D $PtTe_2$ layers/mica samples in the UV-vis wavelength region. The inset shows digital images of a mica substrate before (left) and after (right) the growth of 2D $PtTe_2$ layers by tellurizing 1 nm Pt film. (e) Voltage-dependent IR images of the 2D $PtTe_2$ layers/mica sample corresponding to (d). (f) Voltage-dependent temperature profile obtained from the sample in the inset. (g) Temperature profile obtained from the cyclic application of ON/OFF voltages 50 times.

mittance exhibit high electrical-to-thermal conversion efficiency; *e.g.*, 2D $PtTe_2$ layers prepared by 1 nm Pt with a visible-wavelength transmittance of $\gtrsim$40% (Fig. 2d) exhibit a steep increase of temperature up to ~90 °C at 10 V. These performances are significantly better than those observed with other electro-thermal materials, which will be clarified in the next section. To verify that such excellent electro-thermal performances are substrate-insensitive intrinsic features of our wafer-scale 2D $PtTe_2$ layers, we also directly grew them on optically transparent mica substrates and studied their properties. The inset in Fig. 3d shows images of an identical bare mica substrate before (left) and after (right) tellurizing a Pt film of 1 nm thickness. The main plot in Fig. 3d presents the optical transmittance of the same 2D $PtTe_2$ layers/mica samples exhibiting ~46% transmittance in the visible wavelength range, which is comparable to the observation with the WG-based samples (Fig. 2d). The electro-thermal properties of the same sample were also evaluated, and Fig. 3e shows their representative IR images with increasing voltages. Fig. 3f presents the temperature variation of the same sample as a function of applied voltage and the inset shows the corresponding device image. It is noted that the sample exhibits electro-thermal characteristics nearly similar to those obtained from the 2D $PtTe_2$ layers/WG samples of comparable thickness, *i.e.*, ~90 °C at 10 V for the 1 nm sample in Fig. 3b. This observation indicates that such high-efficiency electro-thermal performances are intrinsic properties of wafer-scale 2D $PtTe_2$ layers achieved by our growth method. Moreover, we evaluated the heating retention capability of the same sample by cyclically applying 0 V (off) and 10 V (on). Fig. 3g presents a variation of temperature obtained during 50 cycles, confirming highly reproducible and reliable electro-thermal retention demanded in practical applications.

Having confirmed their intrinsically excellent electro-thermal properties, we then focused on demonstrating the versatility of 2D $PtTe_2$ layers for a wide range of practical applications, particularly for smart windows. First, we explored a proof-of-concept demonstration of 2D $PtTe_2$ layers for thermochromic displays. Fig. 4a shows a schematic to present the fabrication process of the 2D $PtTe_2$ layer-based thermochromic displays. We first grew 2D $PtTe_2$ layers on WG substrates using the earlier described TAC method and defined metal electrodes on both ends. We then drop-cast a thermochromic ink (purchased from Chameleon®) onto the surface of the 2D $PtTe_2$ layers and printed letters using a silkscreen printing method. Subsequently, we reversibly applied and terminated a constant voltage across the electrodes and monitored the resulting color change. Fig. 4b shows a reversible color change

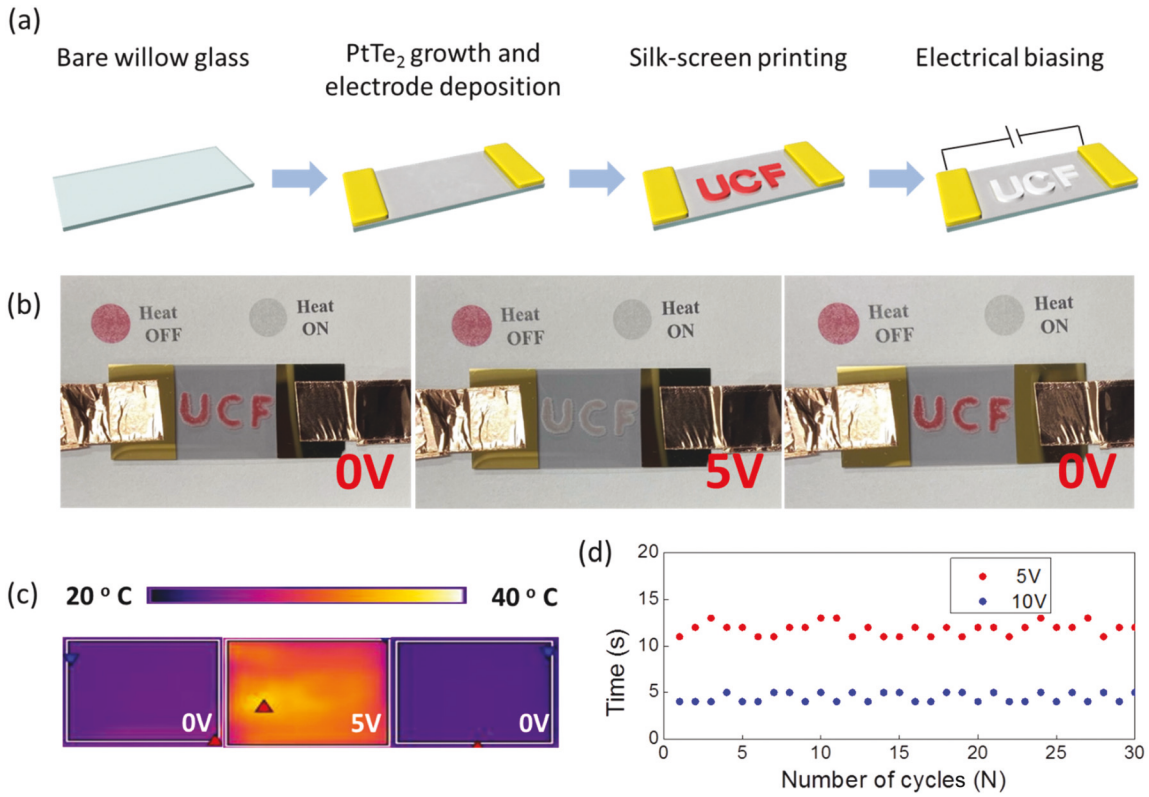

Fig. 4 (a) Schematic diagrams showing the fabrication and operation of the 2D $PtTe_2$ layers/WG-based thermochromic displays. (b) Digital images demonstrating the voltage-driven reversible operation of a thermochromic display at biases of 0 V and 5 V. (c) IR images of the sample corresponding to (b). (d) Cyclic performance of the thermochromic displays at fixed input biases of 5 V and 10 V.

of the printed logo UCF on a 2D $PtTe_2$ layer/WG sample prepared with Pt of 0.7 nm thickness. The logo exhibits translucent-to-red transition upon a reversible application and termination of 5 V through the electrodes, respectively. Fig. 4c shows the IR images of the 2D $PtTe_2$ layers corresponding to Fig. 4b, exhibiting a uniform heat distribution and T_{max} of ~40 °C at 5 V, much higher than the transition temperature of the ink which is 31 °C. Fig. 4d presents the measured time span for the color change obtained at input biases of 5 V and 10 V, which were repeatedly applied for a large number of cycles. The plots confirm that the color change time remains nearly constant at each voltage, *i.e.*, ~12 s for 5 V and ~3 s for 10 V, as well as verify higher electro-thermal efficiency for larger bias. We note that this highly reliable electro-thermal retention of 2D $PtTe_2$ layers outperforms the previously reported graphene-based electro-thermal displays, which exhibit increasing color change time upon repeated measurements.[41]

We explored the application of 2D $PtTe_2$ layers/WG samples for electrically-driven and mechanically-flexible defogging windows. In addition to their combined advantage of intrinsically high electro-thermal efficiency and optical transparency, we studied the surface wettability of 2D $PtTe_2$ layers to verify their stability for defogging applications under humid conditions. Fig. 5a shows the morphological transition of water droplets subsequently integrated on a bare WG (left), after Pt deposition (mid), and its conversion to 2D $PtTe_2$ layers (right). Interestingly, 2D $PtTe_2$ layers exhibit an extremely large water contact angle of 108.27°, a significant increase by ~70° over the bare WG without them on the surface. The high hydrophobicity of the 2D $PtTe_2$ layers is attributed to their low polarity arising from the low electronegativity difference between Pt (~2.28) and Te (~2.10) on the Pauling scale.[42] This intrinsically excellent hydrophobicity of 2D $PtTe_2$ layers suggests implications for self-cleaning surfaces, broadening their versatility for a wide range of applications. Before investigating the defogging performance of 2D $PtTe_2$ layers/WG samples, we first examined the mechanical flexibility of a bare WG by exerting compressive strain. Fig. 5b shows its excellent bendability maintaining the bending radius, R, of ~1.3 cm. As a control experiment for performance comparison, we applied a fog of high relative humidity (*i.e.*, 100%) to a bent bare WG without 2D $PtTe_2$ layers and waited until the fog naturally disappeared at room temperature (Fig. S5, ESI†). We note that the time required for the complete removal of the fog is >3 min. We then performed electro-thermal defogging experiments by using large-area (~5 cm × 2 cm) 2D $PtTe_2$ layers directly grown on WG substrates prepared with Pt of 1.5 nm thickness. A 2D $PtTe_2$ layer/WG sample with Au top electrodes maintaining a bending radius of ~1.3 cm was mounted on top of a humidi-

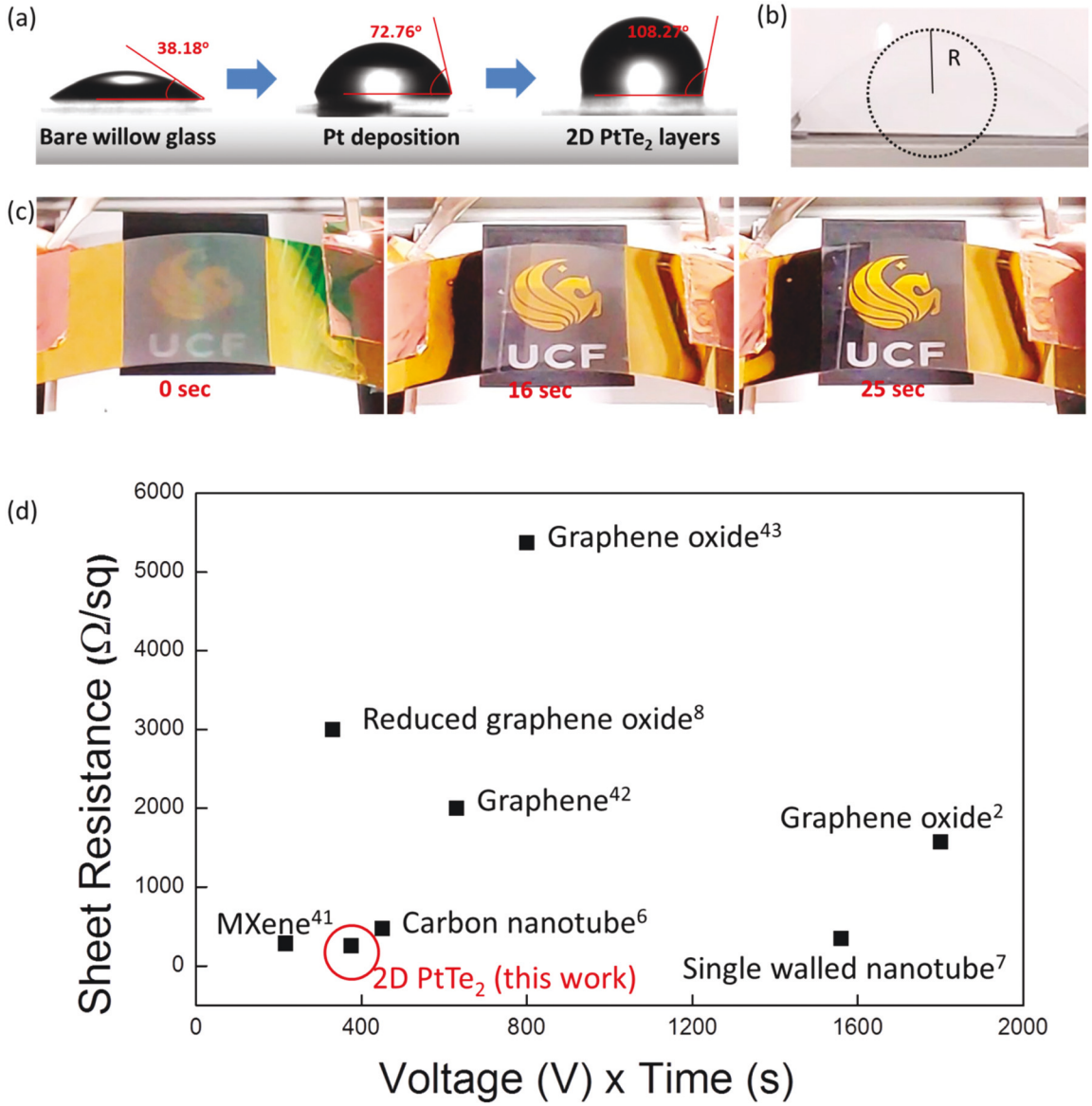

Fig. 5 (a) Water contact angles of a WG substrate in its pristine state, after the deposition of 1.5 nm Pt film and growth of 2D $PtTe_2$ layers (left to right). (b) Image of a WG substrate under compressive strain retaining a bending radius of ~1.3 cm. (c) Demonstration of electrically-driven defogging in a mechanically-flexible 2D $PtTe_2$ layer/WG sample. (d) Performance comparison of various state-of-the-art nanomaterials developed for defogging windows.

fier which produces fog of constant humidity. Subsequently, the Au electrodes were connected by copper tapes and alligator clips through which an input voltage of 15 V was applied using a power supply – well below the safe voltage limit for practical electronic applications. We measured the time span for electrically-biased defogging once the humidity reached 98% which was set to be time-zero. Fig. 5c shows snapshot images of progressive defogging in the mechanically flexible 2D $PtTe_2$ layers/WG samples under 15 V. The underlying UCF logo which was initially invisible became clearly visible after 25 s reaching original transparency indicating complete defogging. For comparison, we also tested the defogging efficiency of the sample without mechanical bending under a lower humidity condition of ~80% and confirmed a fast defogging time of ~7 s (Fig. S6, ESI†). Lastly, we compared the defogging performances of 2D $PtTe_2$ layer-based windows with those of the other previously explored nanomaterials, as presented in Fig. 5d. We note that the 2D $PtTe_2$ layers exhibit the smallest sheet resistance compared to other state-of-the-art nanomaterials adopted in defogging windows – *i.e.*, ~10% smaller than MXenes and ~35% smaller than single-walled carbon nanotubes.[2,6–8,40,41,43,44] Although MXenes exhibit slightly better defogging performance – a smaller value for applied voltage (V) × defogging time (s),[40] their thickness is much larger (*i.e.*, >μm) than that of the 2D $PtTe_2$ layers (thickness: <10 nm, Fig. S2, ESI†) employed for defogging in this study.

Moreover, it is worth mentioning that our defogging experiments were carried out under very high (98%) humidity while humidity conditions for the other materials were not specified in the literature.

Conclusions

In conclusion, we studied the electro-thermal properties of wafer-scale 2D $PtTe_2$ layers and explored them for unconventional smart window applications. We directly grew 2D $PtTe_2$ layers onto glass substrates on a centimeter scale benefiting from their intrinsically low growth temperature. We confirmed that they exhibit extremely high electrical conductivity and electro-thermal conversion efficiency coupled with mechanical flexibility. Demonstrations of thermochromic displays and electrically-operated defogging windows were made utilizing these properties, suggesting the high potential of 2D $PtTe_2$ layers for emerging electro-optical applications.

Conflicts of interest

There are no conflicts to declare.

Acknowledgements

This work was supported by the National Science Foundation (CMMI-1728390) (M. S. S., and Y. J.), the Korea Institute of Energy Technology Evaluation and Planning (KETEP) and the Ministry of Trade, Industry & Energy (MOTIE) of the Republic of Korea (No. 20173010013340) (Y. J.). Y. J. also acknowledges the VPR Advancement of Early Career Researchers award from the University of Central Florida. This research was in part supported by the Creative Materials Discovery Program through the National Research Foundation of Korea (NRF) funded by the Ministry of Science, ICT and Future Planning (NRF-2017M3D1A1039553).

Notes and references

1 J. H. Kim, B. D. Ahn, C. H. Kim, K. A. Jeon, H. S. Kang and S. Y. Lee, *Thin Solid Films*, 2008, **516**, 1330–1333.
2 D. Sui, Y. Huang, L. Huang, J. Liang, Y. Ma and Y. Chen, *Small*, 2011, **7**, 3186–3192.
3 U. Bach, D. Lupo, P. Comte, J. E. Moser, F. Weissörtel, J. Salbeck, H. Spreitzer and M. Grätzel, *Nature*, 1998, **395**, 583–585.
4 X. Wang, L. Zhi and K. Müllen, *Nano Lett.*, 2008, **8**, 323–327.
5 K. S. Kim, Y. Zhao, H. Jang, S. Y. Lee, J. M. Kim, K. S. Kim, J.-H. Ahn, P. Kim, J.-Y. Choi and B. H. Hong, *Nature*, 2009, **457**, 706–710.
6 L. R. Shobin and S. Manivannan, *Sol. Energy Mater. Sol. Cells*, 2018, **174**, 469–477.
7 B. Zhou, X. Han, L. Li, Y. Feng, T. Fang, G. Zheng, B. Wang, K. Dai, C. Liu and C. Shen, *Compos. Sci. Technol.*, 2019, **183**, 107796–107803.
8 H. Sun, D. Chen, C. Ye, X. Li, D. Dai, Q. Yuan, K. W. A. Chee, P. Zhao, N. Jiang and C.-T. Lin, *Appl. Surf. Sci.*, 2018, **435**, 809–814.
9 B. Mortazavi, M. Shahrokhi, M. Raeisi, X. Zhuang, L. F. C. Pereira and T. Rabczuk, *Carbon*, 2019, **149**, 733–742.
10 S. Manivannan, J. H. Ryu, J. Jang and K. C. Park, *J. Mater. Sci.: Mater. Electron.*, 2010, **21**, 595–602.
11 G. Wang, L. Bi, W. Wei, X. Zhang, Y. Gu, L. Huang, H. Yin, Y. Li, G. Chen, Z. Wu and C. Ye, *ACS Appl. Nano Mater.*, 2019, **2**, 6707–6714.
12 H. S. Kang, J. Choi, W. Cho, H. Lee, D. Lee, D. G. Lee and H.-T. Kim, *J. Mater. Chem. C*, 2016, **4**, 9834–9840.
13 Y. Jin, D. Deng, Y. Cheng, L. Kong and F. Xiao, *Nanoscale*, 2014, **6**, 4812–4818.
14 W. Xiong, H. Liu, Y. Chen, M. Zheng, Y. Zhao, X. Kong, Y. Wang, X. Zhang, X. Kong, P. Wang and L. Jiang, *Adv. Mater.*, 2016, **28**, 7167–7172.
15 G. R. Bhimanapati, Z. Lin, V. Meunier, Y. Jung, J. Cha, S. Das, D. Xiao, Y. Son, M. S. Strano, V. R. Cooper, L. Liang, S. G. Louie, E. Ringe, W. Zhou, S. S. Kim, R. R. Naik, B. G. Sumpter, H. Terrones, F. Xia, Y. Wang, J. Zhu, D. Akinwande, N. Alem, J. A. Schuller, R. E. Schaak, M. Terrones and J. A. Robinson, *ACS Nano*, 2015, **9**, 11509–11539.
16 L. Gao, *Small*, 2017, **13**, 1603994–1604018.
17 Q. H. Wang, K. Kalantar-Zadeh, A. Kis, J. N. Coleman and M. S. Strano, *Nat. Nanotechnol.*, 2012, **7**, 699–712.
18 M. Chhowalla, H. S. Shin, G. Eda, L.-J. Li, K. P. Loh and H. Zhang, *Nat. Chem.*, 2013, **5**, 263–275.
19 H. Ma, P. Chen, B. Li, J. Li, R. Ai, Z. Zhang, G. Sun, K. Yao, Z. Lin, B. Zhao, R. Wu, X. Tang, X. Duan and X. Duan, *Nano Lett.*, 2018, **18**, 3523–3529.
20 C. S. Boland, C. Ó. Coileáin, S. Wagner, J. B. McManus, C. P. Cullen, M. C. Lemme, G. S. Duesberg and N. McEvoy, *2D Mater.*, 2019, **6**, 045029–045037.
21 S. Hao, J. Zeng, T. Xu, X. Cong, C. Wang, C. Wu, Y. Wang, X. Liu, T. Cao, G. Su, L. Jia, Z. Wu, Q. Lin, L. Zhang, S. Yan, M. Guo, Z. Wang, P. Tan, L. Sun, Z. Ni, S.-J. Liang, X. Cui and F. Miao, *Adv. Funct. Mater.*, 2018, **28**, 1803746–1803754.
22 Q. Ji, C. Li, J. Wang, J. Niu, Y. Gong, Z. Zhang, Q. Fang, Y. Zhang, J. Shi, L. Liao, X. Wu, L. Gu, Z. Liu and Y. Zhang, *Nano Lett.*, 2017, **17**, 4908–4916.
23 A. T. Neal, Y. Du, H. Liu and P. D. Ye, *ACS Nano*, 2014, **8**, 9137–9142.
24 R. Gatensby, T. Hallam, K. Lee, N. McEvoy and G. S. Duesberg, *Solid-State Electron.*, 2016, **125**, 39–51.
25 S. S. Han, J. H. Kim, C. Noh, J. H. Kim, E. Ji, J. Kwon, S. M. Yu, T.-J. Ko, E. Okogbue, K. H. Oh, H.-S. Chung, Y. Jung, G.-H. Lee and Y. Jung, *ACS Appl. Mater. Interfaces*, 2019, **11**, 13598–13607.
26 E. Okogbue, J. H. Kim, T.-J. Ko, H.-S. Chung, A. Krishnaprasad, J. C. Flores, S. Nehate, M. G. Kaium,

J. B. Park, S.-J. Lee, K. B. Sundaram, L. Zhai, T. Roy and Y. Jung, *ACS Appl. Mater. Interfaces*, 2018, **10**, 30623–30630.
27 E. Okogbue, S. S. Han, T.-J. Ko, H.-S. Chung, J. Ma, M. S. Shawkat, J. H. Kim, J. H. Kim, E. Ji, K. H. Oh, L. Zhai, G.-H. Lee and Y. Jung, *Nano Lett.*, 2019, **19**, 7598–7607.
28 M. Yan, H. Huang, K. Zhang, E. Wang, W. Yao, K. Deng, G. Wan, H. Zhang, M. Arita, H. Yang, Z. Sun, H. Yao, Y. Wu, S. Fan, W. Duan and S. Zhou, *Nat. Commun.*, 2017, **8**, 257–262.
29 N. Choudhary, H.-S. Chung, J. H. Kim, C. Noh, M. A. Islam, K. H. Oh, K. Coffey, Y. Jung and Y. Jung, *Adv. Mater. Interfaces*, 2018, **5**, 1800382–1800390.
30 M. A. Islam, J. Church, C. Han, H.-S. Chung, E. Ji, J. H. Kim, N. Choudhary, G.-H. Lee, W. H. Lee and Y. Jung, *Sci. Rep.*, 2017, **7**, 14944–14653.
31 M. S. Shawkat, H.-S. Chung, D. Dev, S. Das, T. Roy and Y. Jung, *ACS Appl. Mater. Interfaces*, 2019, **11**, 27251–27258.
32 J. H. Kim, T.-J. Ko, E. Okogbue, S. S. Han, M. S. Shawkat, M. G. Kaium, K. H. Oh, H.-S. Chung and Y. Jung, *Sci. Rep.*, 2019, **9**, 1641.
33 L. Fu, D. Hu, R. G. Mendes, M. H. Rummeli, Q. Dai, B. Wu, L. Fu and Y. Liu, *ACS Nano*, 2018, **12**, 9405–9411.
34 A. Glamazda, K. Y. Choi, P. Lemmens, J. J. Yang and S. W. Cheong, *New J. Phys.*, 2014, **16**, 093061–093073.
35 A. Politano, G. Chiarello, C.-N. Kuo, C. S. Lue, R. Edla, P. Torelli, V. Pellegrini and D. W. Boukhvalov, *Adv. Funct. Mater.*, 2018, **28**, 1706504–1706511.
36 C. Yim, K. Lee, N. McEvoy, M. O'Brien, S. Riazimehr, N. C. Berner, C. P. Cullen, J. Kotakoski, J. C. Meyer, M. C. Lemme and G. S. Duesberg, *ACS Nano*, 2016, **10**, 9550–9558.
37 P. Kang, M. C. Wang, P. M. Knapp and S. Nam, *Adv. Mater.*, 2016, **28**, 4639–4645.
38 S. Yang, H. Cai, B. Chen, C. Ko, V. O. Özçelik, D. F. Ogletree, C. E. White, Y. Shen and S. Tongay, *Nanoscale*, 2017, **9**, 12288–12294.
39 L. Tan, M. Zeng, Q. Wu, L. Chen, J. Wang, T. Zhang, J. Eckert, M. H. Rümmeli and L. Fu, *Small*, 2015, **11**, 1840–1846.
40 T. H. Park, S. Yu, M. Koo, H. Kim, E. H. Kim, J.-E. Park, B. Ok, B. Kim, S. H. Noh, C. Park, E. Kim, C. M. Koo and C. Park, *ACS Nano*, 2019, **13**, 6835–6844.
41 J. Sun, Y. Chen, M. K. Priydarshi, Z. Chen, A. Bachmatiuk, Z. Zou, Z. Chen, X. Song, Y. Gao, M. H. Rümmeli, Y. Zhang and Z. Liu, *Nano Lett.*, 2015, **15**, 5846–5854.
42 M. Wang, T.-J. Ko, M. S. Shawkat, S. S. Han, E. Okogbue, H.-S. Chung, T.-S. Bae, S. Sattar, J. Gil, C. Noh, K. H. Oh, Y. Jung, J. A. Larsson and Y. Jung, *ACS Appl. Mater. Interfaces*, 2020, **12**, 10839–10851.
43 J. Wang, Z. Fang, H. Zhu, B. Gao, S. Garner, P. Cimo, Z. Barcikowski, A. Mignerey and L. Hu, *Thin Solid Films*, 2014, **556**, 13–17.
44 Z. Wang, Z. Xue, M. Zhang, Y. Wang, X. Xie, P. K. Chu, P. Zhou, Z. Di and X. Wang, *Small*, 2017, **13**, 1700929–1700936.